Journal of the Mechanics and Physics of Solids 88 (2016) 186–203

Contents lists available at ScienceDirect

Journal of the Mechanics and Physics of Solids

journal homepage: www.elsevier.com/locate/jmps

A molecular informed poroelastic model for organic-rich, naturally occurring porous geocomposites

Siavash Monfared, Franz-Josef Ulm*

Department of Civil and Environmental Engineering, Massachusetts Institute of Technology, Cambridge, MA, USA

ARTICLE INFO

Article history:
Received 9 July 2015
Received in revised form
11 November 2015
Accepted 14 December 2015
Available online 28 December 2015

Keywords:
Poroelasticity
Imperfect interface
Organic-rich shale
Organic maturity
Partial rank correlation coefficient
Microtexture

ABSTRACT

Molecular simulation results on organic maturity (mature and immature kerogen as the two asymptotic cases) are introduced into a continuum micromechanics based model for organic-rich shales. Through a fundamental functional relationship that constrains microporous kerogen density and elasticity variable spaces and within the framework of effective media theory; the model bridges the gap between asymptotic cases of organic maturity with texture as the overriding theme, specifically a matrix/inclusion (Mori–Tanaka) texture for immature systems and a granular (self-consistent) texture for mature ones. The utility of the molecular results merged into a continuum framework is demonstrated by estimating kerogen's microporosity (<2 nm) from nanoindentation measurements. The effect of burial and diagenetic processes on the effective poroelasticity of these porous, naturally occurring geocomposites are captured by introduction of imperfect interfaces. Finally, the performance of the model is fully characterized by ranking the normalized contribution of uncertainty of input to the overall behavior and parameters of interest to geophysicists and geomechanicians such as degree of anisotropy and *in situ* stresses.

1. Introduction

Due to their abundance, organic-rich shales are playing a critical role in re-defining the world's energy landscape and in re-formulating the global geopolitics. However, technological challenges and environmental concerns continue to contribute to the slow growth of organic-rich shale exploration and exploitation worldwide. The highly heterogeneous nature and anisotropic behavior (mechanical and transport) of these porous organic/inorganic composites leave many open questions regarding their characterization, modeling and engineering design. Our objective is to link organic maturity and its elasticity to the effective elastic and poroelastic behavior of these intricate, naturally occurring geocomposites with texture as the overriding theme. The significant body of literature on modeling shales and organic-rich shales (see e.g. Vernik and Nur, 1992; Hornby et al., 1994; Ulm et al., 2004; Ortega et al., 2009b; Vernik and Kachanov, 2010; Sayers, 2013; Khadeeva and Vernik, 2014); does not explore the effect of organic maturity on the overall poroelastic behavior of these source rocks. In addition, the elasticity and the density of the organics are often assumed *a priori*; failing to account for variations in structural, physical and chemical properties of these organics.

In a hypothesis testing approach, we attribute the first-order contribution of organic maturity on overall elasticity for low total organic carbon (TOC $\leq$1 mass%) shales to a texture effect while for high TOC systems, kerogen elastic properties assume

---

* Corresponding author.
E-mail address: ulm@mit.edu (F.-J. Ulm).

http://dx.doi.org/10.1016/j.jmps.2015.12.006
0022-5096/© 2015 Elsevier Ltd. All rights reserved.

a role of first-order nature. Assuming all organics to be microporous kerogen, we utilize a functional relationship obtained from molecular simulations on these microporous organics (Bousige et al., 2015) to constrain kerogen stiffness and its density variable spaces; avoiding any assumptions *a priori* for these parameters. The simulations of Bousige et al. (2015) were performed on re-constructed microporous kerogen samples and thus the kerogen phase referred throughout this work is a microporous organic solid. The elastic and the fracture behavior of three re-constructed microporous kerogen samples with different levels of maturity using a hybrid experimental-simulation technique were explored by Bousige et al. (2015). Their results suggest that kerogen's Poisson's ratio has a low sensitivity with respect to its density and the state of maturity. A nearly constant ($\nu^{\text{kerogen}} \approx 0.25$) Poisson's ratio from molecular simulations of Bousige et al. (2015) leaves one degree of freedom associated with the isotropic elasticity of kerogen that is constrained through a fundamental functional relationship with the density of kerogen, ρ^{kerogen} (see Fig. 6). The low sensitivity of ν^{kerogen} to the state of maturity seems to be a consequence of the amorphous structure of kerogen and the randomness of the network that connects these organic macromolecules.

As an application we estimate kerogen's microporosity from elastic measurements, in this case instrumented nanoindentation data. The incorporation of the molecular simulation results into a mean field based framework shows promise in providing an unprecedented insight into subsurface rock properties from elastic based measurements e.g. seismic and sonic wave velocities.

Lastly, we employ Spearman's partial rank correlation coefficient (SPRCC) to fully characterize the sensitivity of our model to uncertainty in input parameters. The results can be of interest to geoscientists to better manage confidence in their calculations by characterizing parameters with the highest contribution.

2. Theoretical tools

2.1. Homogenization and inclusion based effective estimates

The fourth-order homogenized stiffness tensor, $\mathbb{C}^{\text{hom}}$, associated with a defined representative elementary volume, *rev*, denoted by Ω, can be obtained from (Zaoui, 2002):

$$\mathbb{C}^{\text{hom}} = \left\langle \mathbb{C}^r\left(\underline{x}\right) : \mathbb{A}^r\left(\underline{x}\right) \right\rangle_{\Omega} \quad \forall\ \underline{x} \in \Omega \tag{1}$$

where $\langle \cdots \rangle_\Omega$ implies volume averaging over Ω and $\Omega = \Omega^1 \cup \Omega^2 \cup \Omega^3 \cup \cdots \cup \Omega^r$ where Ω^r represents the rth subdomain, all mutually exclusive. The scale separability condition requires the characteristic size of a micro-homogeneous phase in Ω, denoted by d, to be much smaller than the characteristic length of the *rev*, ℓ, for homogenization (Zaoui, 2002). $\mathbb{C}^r$ is the stiffness tensor of the rth micro-homogeneous phase and $\mathbb{A}^r$ is the fourth-order strain localization tensor. Due to Eshelby's celebrated solution (Eshelby, 1957), in linear elasticity one can define the strain concentration tensor for phase r, $\mathbb{A}^r$, as follows (Dormieux et al., 2006):

$$\mathbb{A}^r = \left[\mathbb{I} + \mathbb{P} : \left(\mathbb{C}^r - \mathbb{C}^0\right)\right]^{-1} : \left\langle \left[\mathbb{I} + \mathbb{P} : \left(\mathbb{C}^r - \mathbb{C}^0\right)\right]^{-1} \right\rangle_{\Omega}^{-1} \tag{2}$$

where $\mathbb{I} = I_{ijkl} = \frac{1}{2}(\delta_{ik}\delta_{jl} + \delta_{il}\delta_{ik})$ is the fourth-order identity tensor, $\mathbb{C}^0$ denotes the background matrix stiffness tensor, and $\mathbb{P}$ is the fourth-order Hill concentration tensor. The generalized expression for Hill concentration tensor reads (Zaoui, 2002):

$$P_{ijkl} = -\left(\frac{\partial^2}{\partial x_j \partial x_l} \int_{\Omega} G_{ik}\left(\underline{x} - \underline{x}'\right) d\Omega\right)_{(ij)(kl)} \tag{3}$$

with $(ij)(kl)$ implying indices symmetrization and $G_{ij}(\underline{x} - \underline{x}')$ representing the second order Green's tensor for a generalized linear, elastic, anisotropic medium that characterizes displacement at point $\underline{x}$due to a Dirac delta type point force at $\underline{x}'$. Hill concentration tensor is related to Eshelby tensor, $\mathbb{S}^{\text{Esh}}$, in the following way:

$$\mathbb{S}^{\text{Esh}} = \mathbb{P} : (\mathbb{C}^0)^{-1} \tag{4}$$

There are different ways to approximate Eq. (2) since aside from volume fractions, statistical distribution of higher order textural parameters is almost never available for a random media. The two approximation schemes, with some physically meaningful interpretations, are the self-consistent and the Mori–Tanaka. The self-consistent approximation scheme was introduced and developed by Hershey (1954), Kroner (1958), Budiansky (1965) and Hill (1965). In the self-consistent scheme, $\mathbb{C}^0$ in Eq. (2) is set equal to $\mathbb{C}^{\text{hom}}$ resulting in an implicit expression. This implies that no particular phase plays a dominant role in contributing to the effective stiffness of the composite. The Mori–Tanaka approximation scheme was initially proposed by Mori and Tanaka (1973) and further developed by Beneviste (1987). The Mori–Tanaka approximation scheme can be achieved by setting $\mathbb{C}^0$ in Eq. (2) equal to $\mathbb{C}^M$, where $\mathbb{C}^M$ is the stiffness of the dominant matrix phase. Mori–Tanaka is often associated with a “swiss-cheese”/matrix-inclusion texture.

2.2. Imperfect interfaces

In most continuum mechanics treatments, interfaces are assumed to be perfect. However, in reality, interfaces may play a significant role on the effective elasticity of a composite. Thus, typical continuum mechanics approaches need to get refined by accounting for the presence of these imperfect interfaces. The interface model employed here introduces a spring layer of vanishing thickness, with a characteristics compliance, $\omega_{ij} = \alpha\delta_{ij} + (\beta - \alpha)n_i n_j$, between the inclusion (Ω_{inc}) and the matrix (Qu, 1993a,b). Decomposing ω_{ij} into tangential, α, and normal, β, components allows one to consider relative sliding. One can recover a perfect interface, i.e. full bonding between the inclusion and the matrix, by setting $\omega_{ij}=0$, while $\omega_{ij}\longrightarrow\infty$ represents a complete de-bonding between inclusion and matrix.

Eshelby's solution (Eshelby, 1957) for total strain in an ellipsoidal inclusion can be refined to account for imperfect bonding by introducing a surface integral over the interface to collect contributions due to interface “imperfections” (Qu, 1993b). The modified Eshelby tensor for an ellipsoidal inclusion, $\mathbb{S}^{\mathrm{MEsh}}$, for small ω, i.e. slightly weakened interface, reads (Qu, 1993b):

$$S^{\mathrm{MEsh}}_{ijkl} = \frac{1}{|\Omega_{\mathrm{inc}}|}\int_{\Omega_{\mathrm{inc}}} S^{\mathrm{Esh}}_{ijkl}(\underline{x})\,d\Omega_{\mathrm{inc}}(\underline{x}) = S^{\mathrm{Esh}}_{ijkl} + (I_{ijpq} - S^{\mathrm{Esh}}_{ijpq}) \times H_{pqrs}C_{rsmn}(I_{mnkl} - S^{\mathrm{Esh}}_{mnkl}) \tag{5}$$

where $H_{ijkl} = \alpha T_{ijkl} + (\beta - \alpha)Q_{ijkl}$ embeds the interface compliance. For the special case of spheroidal inclusions, $T_{ijkl} = \frac{1}{a}(I_{ijkl})$ and $Q_{ijkl} = \frac{1}{5a}(2I_{ijkl} + \delta_{ij}\delta_{kl})$ (Qu, 1993a). The inclusion grain radius, ‘a’, introduces a length scale into our continuum micromechanical model. Finally, invoking Eq. (4), one can obtain the modified Hill concentration tensor, $\mathbb{P}^M$:

$$\mathbb{P}^M = \mathbb{S}^{\mathrm{MEsh}} : \left(\mathbb{C}^0\right)^{-1} \tag{6}$$

The modified Hill concentration tensor allows us to account for imperfect (to be precised: slightly weakened) interfaces in our micromechanics based framework.

3. Materials

The model was calibrated and validated with two comprehensive data sets belonging to Woodford (A1–A5) (Abousleiman et al., 2007; Bobko, 2008) and Haynesville (B1–B6) shales. The Woodford samples are classified as immature (Romero and Philp, 2012) while the Haynesville samples are considered to be mature from RockEval analysis (Hydrogen Index (HI) =17 S2 × 100/TOC and Oxygen Index (OI) =9 S3 × 100/TOC). For calibration, macroscopic elasticity is utilized while the validation step employs nanoindentation data on the same samples. The mineralogy, porosity, organic content and macroscopic elasticity used for calibration in addition to measured indentation data employed for validation are summarized in Table A1 and Table A2, respectively. The utility of our original modeling approach is demonstrated through estimation of kerogen's bulk modulus, K^{kerogen}, ρ^{kerogen}, and kerogen's microporosity, φ^{micro}, from elasticity; in this case nanoindentation data on samples from Barnett (C1), Antrim (D1), Marcellus (F1–F5) and Fayetteville (G1). The mineralogy of these samples,

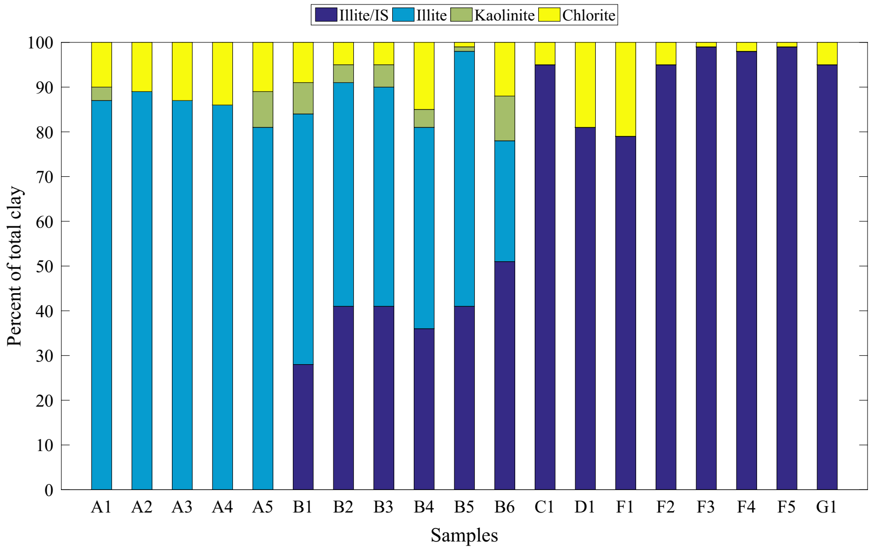

Fig. 1. Clay type distribution in the studied samples. Illite is the main clay component in all the samples used in this study. Illite/IS stands for mixed layers of illite–smectite.

Table 1
Linear thermal expansion coefficients for various geomaterials.

Material	α_{Th} [(mm/m)/, C°]
Degassed charcoal[a]	4.50
Charcoal (glassy)[b]	4 ± 0.1
Charcoal (rubbery)[b]	6 ± 1
Green River kerogen-MD simulation[c]	292 ± 25
Green River Kerogen-Experiment[c]	104 ± 8
Kaolinite (x_3)[d]	18.6 ± 1.3
Kaolinite (x_1)[d]	5.2 ± 1.7
Chlorite (x_3)[d]	9 ± 2.3
Chlorite (x_3)[d]	11.1 ± 1.4
α-Quartz[e]	24.3
Feldspar[e]	14.1-15.6

[a] Bangham and Franklin (1946).
[b] Zhang et al. (2007).
[c] Zhang and Leboeuf (2007).
[d] McKinstry (1965).
[e] Houtari and Kukkonen (2004).

porosity and organic content as well as measured indentation modulus (Abedi et al., 2015) are summarized in Table B1 and Table B2, respectively. Fig. 1 shows the distribution of different clay types for all data, hinting at the dominance of illite.

4. Model developments

The poroelastic behavior of any porous composite can be described by the classical poroelastic state equations (Dormieux et al., 2006):

$$\boldsymbol{\Sigma} = \mathbb{C}^{\text{hom}} : \mathbf{E} - \boldsymbol{\alpha} p \tag{7}$$

$$(\phi - \phi_0) = \boldsymbol{\alpha} : \mathbf{E} + \frac{p}{N} \tag{8}$$

$(\phi - \phi_0)$ is the Lagrangian porosity change, $\boldsymbol{\alpha}$ denotes the second-order tensor of Biot pore pressure coefficients, and N is the solid Biot modulus. In what follows, we will first present a structural and textural thought model which forms the backbone for our model development. Then, the expressions for the effective stiffness and the poroelastic constants are presented.

4.1. Structural and microtextural thought model

We consider a multi-scale thought model that allows us to define a representative elementary volume (*rev*) at each considered length scale following the framework established by Ulm et al. (2004) and its continuation by Ortega et al. (2009b). The building block of the model, at level 0, is considered to be a microporous kerogen. Level I of the model corresponds to the length scale associated with nanoindentation (10^{-7}–10^{-6} m) with its *rev* denoted by Ω_I associated with the composite response of a porous inorganic phase, i.e. clay, and a porous organic phase, i.e. kerogen. The effective stiffness associated with this porous composite is denoted by $\mathbb{C}_I^{\text{hom}}$. Anisotropy is introduced to the model as an intrinsic characteristic of clay with its stiffness, $\mathbb{C}^{\text{clay}}$, considered to be transversely isotropic with x_3 parallel to the axis of rotational symmetry and x_1 parallel to the direction of the bedding planes. For the immature system, all measured porosity is assumed to be in the clay phase while microporous kerogen forms a continuous matrix leading to a matrix/inclusion texture and thus a Mori–Tanaka homogenization scheme. The measured porosity does not include the micropores of the kerogen phase. As maturity progresses, kerogen pockets are reduced in size and become dispersed in the matrix (Prasad et al., 2009; Ahmadov, 2011). This implies more contact between stiff inorganic components leading to a continuous set of possible contact forces, characteristic of a granular system (Radjai et al., 1996), best captured by a self-consistent homogenization scheme (Ulm and Abousleiman, 2006). As a consequence of a self-consistent texture, porosity in mature system is assumed to be self-consistently distributed, in both organic and inorganic phases. This implies that all solid phases in each level of the model possess the same porosity. This is consistent with experimental observations suggesting the prevalence of porosity in mature kerogen relative to immature ones (Curtis et al., 2013). In the case of mature system, the self-consistent distribution of porosity leads to additional porosity in the microporous kerogen phase. Moreover, while characterizing pore size distribution (PSD) to validate their molecular model for mature and immature kerogen with experimental PSD, Bousige et al. (2015) report that mature samples possess larger pores (pore size > 2 nm) compared to immature ones.

Vernik and Kachanov (2010) report that Mori–Tanaka scheme is a powerful tool for capturing poorly consolidated sands. Indeed, one can think of kerogen maturation as a "consolidation" process induced not by physical but chemical processes since the process of kerogen maturation entails a volume change in the organics phase, a phenomenon that has been extensively studied (see e.g. Yakobson, 1991; Malthe-Srenssen et al., 2006). At level II of the model with its *rev* denoted by Ω_{II}, we account for the contribution of silt inclusions to the effective elasticity. This level of the model corresponds to a length scale of relevance to sonic and ultra-sonic frequencies (10^{-7}–10^{-6} m). The stiffness associated with this level of the model is denoted by $\mathbb{C}_{\text{II}}^{\text{hom}}$. A literature survey on mechanical characterization of organic-rich shales suggests the prevalence of discontinuities in mature organic-rich shales relative to immature ones (see e.g. Vernik and Nur, 1992; Vernik, 1993; Vernik and Landis, 1996; Vernik and Xingzhou, 1997). In addition, it has been observed that texture has a more significant contribution to velocity anisotropy compared to micro-cracks (Prasad et al., 2009). To account for the presence of discontinuities and microtextural anisotropy, we introduce imperfect interfaces between silt inclusion grains and its surrounding matrix in the mature system. The rational for existence of imperfect interfaces can be further explored by considering the expression for radial stresses in a thermoelastic formulation between the interface of a matrix and an inclusion:

$$\sigma_{rr}(r=a) = \frac{3K^{\text{inc}} \times 4G^{M}}{3K^{\text{inc}} + 4G^{M}} \left(\alpha_{\text{Th}}^{M} - \alpha_{\text{Th}}^{\text{inc}}\right) \Delta\theta \tag{9}$$

A positive value of radial stress, σ_{rr}, at the inclusion/matrix boundary, i.e. $r=a$, implies a tensile stress field. Here, superscripts M and inc denote quantities associated with matrix and inclusions, respectively. α_{Th} represent the coefficient of

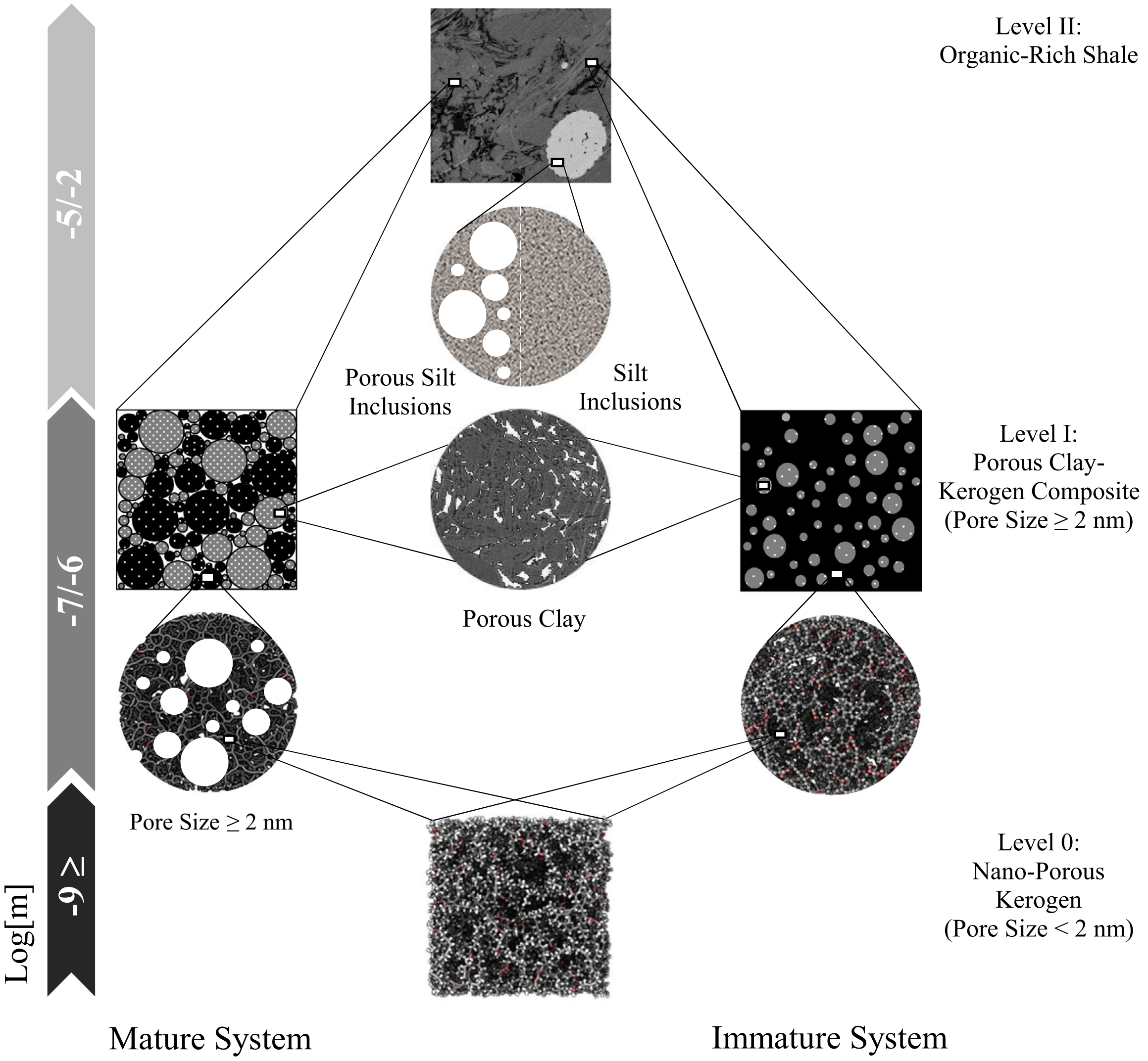

Fig. 2. Schematics for the multi-scale maturity dependent model for organic-rich shales. At level 0, microporous kerogen forms the building block of the model. Level I of the model corresponds to the length scale relevant to nanoindentation representing the composite response of porous clay and porous kerogen phases (different porosity distributions for each system); homogenized in intermediary homogenization steps, each shown by a circle. The macroscopic response, level II of the model, is captured by accounting for the contribution of inclusion silt grains to the effective poroelasticity. The self-consistent texture of mature systems implies a self-consistent porosity distribution in each phase, as shown on the left side of this schematics.

linear thermal expansion and $\Delta\theta$ is the change in temperature. Assuming that change of temperature is positive during burial/diagentic processes over geological times (i.e. $\Delta\theta > 0$), one can readily see that a positive radial stress occurs when thermal expansion of the matrix becomes larger than that of the inclusion, producing a tensile stress field. Characteristic values of thermal expansion coefficients for some constituent of organic-rich shale are given in Table 1. For inclusions, taking charcoal as an asymptotic case for mature kerogen and Green River, an immature example, as well as kaolinite as the mineral making up the inorganic matrix; one can readily observe that at some point in geological times, the physical and chemical changes in kerogen structure and composition lead to $(\alpha_{\text{Th}}^{M} - \alpha_{\text{Th}}^{in}) > 0$ which in turn leads to partial de-bonding at the interfaces between organic and inorganic constituents. This illustrates the significance of burial/diagenetic processes on overall anisotropic poroelasticity of organic-rich shales. Finally, in our approach, we consider grains and pores to be spheroidal. This is based on the notion that aspect ratios and grain orientations do not seem to have a first-order contribution on the overall poroelastic behavior of organic-rich shales, specifically in a porous solid with a high packing density (Ortega et al., 2009a). Vernik and Kachanov (2010) argue that in seismic and sonic frequency range for low porosity rocks, i.e. high solid packing density, (pore or crack) aspect ratios do not play a significant role.

In summary, for immature systems, $\Omega_{\text{I}} = \Omega_{\text{pc}} \cup \Omega_{\text{kerogen}}$ and $\Omega_{\text{II}} = \Omega_{\text{I}}^{\text{up}} \cup \Omega_{\text{inc}}$. Similarly, for the mature case, $\Omega_{\text{I}} = \Omega_{\text{pc}} \cup \Omega_{\text{pk}}$ and $\Omega_{\text{II}} = \Omega_{\text{I}} \cup \Omega_{\text{pinc}}$. Porous clay is denoted by ‘pc’, porous kerogen is represented by ‘pk’, porous inclusion is shown by ‘pinc’ and $\Omega_{\text{I}}^{\text{up}}$ is the upscaled poroelastic response of Ω_{I} which is homogenized with porous inclusions. The schematic representation of the model is shown in Fig. 2.

4.2. Volume fractions

4.2.1. Immature system

Based on the thought model presented in Section 4.1, the volume fractions associated with the phases that contribute to the poroelastic behavior of organic-rich shales at macroscopic length scale can be written as: $f^{\text{clay}} + f^{\text{kerogen}} + f^{\text{inc}} + \phi = 1$. The measured porosity is denoted by ϕ while $f^{\text{clay}}, f^{\text{kerogen}}$ and f^{inc} represent volume fractions associated with clay, kerogen and silt inclusion phases, respectively. The volume fraction of the rth solid phase at level II is defined as:

$$f^r = (1 - \phi)\frac{m^r/\rho_g^r}{\sum_{i=1}^{p} m^i/\rho_g^i} \tag{10}$$

where m^r is the mass percent of the rth phase, ρ_g^r is the grain density associated with this phase and p stands for all minerals present plus kerogen. The silt grain inclusion volume fraction, f^{inc}, consists of all inorganic minerals excluding clay. It is defined as follows:

$$f^{\text{inc}} = (1 - \phi)\frac{\sum_{j=1}^{k} m^j/\rho_g^j}{\sum_{i=1}^{p} m^i/\rho_g^i} \tag{11}$$

with k representing all none clay inorganics (silt grains). At level I of the model, the solid volume fraction associated with the rth solid phase, η^r, reads:

$$\eta^r = \frac{f^r}{1 - f^{\text{inc}}} \tag{12}$$

And similarly, porosity at level I, φ reads:

$$\varphi = \frac{\phi}{1 - f^{\text{inc}}} \tag{13}$$

Furthermore, in order to estimate $\mathbb{C}_{\text{pc}}$ associated with Ω_{pc}; we define the following volume fractions: $\eta_n^{\text{clay}} = \frac{\eta^{\text{clay}}}{\eta^{\text{clay}} + \varphi}$ and $\varphi_n = \frac{\varphi}{\eta^{\text{clay}} + \varphi}$.

4.2.2. Mature system

For the mature model, granular microtexture and consequently a self-consistent porosity distribution result in a slightly different set of definitions for volume fractions. The volume fractions corresponding to the phases that contribute to the poroelastic behavior of mature organic-rich shale macroscopically are: $f^{\text{clay}} + f^{\text{kerogen}} + f^{\text{inc}} + \phi^{\text{inc}} + \phi^{\text{ker}} + \phi^{\text{clay}} = 1$; where:

$$\phi^r = \frac{f^r}{f^{\text{inc}} + f^{\text{ker}} + f^{\text{clay}}}\phi \tag{14}$$

The measured porosity, $\phi = \phi^{\text{clay}} + \phi^{\text{kerogen}} + \phi^{\text{inc}}$ where ϕ^r (r=inc, kerogen, clay) is the self-consistent porosity associated with the solid phases. f^{clay} and f^{kerogen} are defined by Eq. (10) while f^{inc} is expressed by Eq. (11). The solid volume fraction of the rth phase, η^r, and the porosity, φ, at level I of the model can be obtained from:

$$\eta^r = \frac{f^r}{1 - f^{\text{pinc}}} \tag{15}$$

$$\varphi^r = \frac{\phi^r}{1 - f^{\text{pinc}}} \tag{16}$$

Where $f^{\text{pinc}} = f^{\text{inc}} + \phi^{\text{inc}}$. Additionally, the normalized kerogen volume fraction and the porosity associated with domain Ω_{pk} is defined as: $\eta_n^{\text{kerogen}} = \frac{\eta^{\text{kerogen}}}{\eta^{\text{kerogen}} + \varphi^{\text{kerogen}}}$ and $\varphi_n^{\text{kerogen}} = \frac{\varphi^{\text{kerogen}}}{\eta^{\text{kerogen}} + \varphi^{\text{kerogen}}}$. For the domain associated with porous clay, Ω_{pc}, $\eta_n^{\text{clay}} = \frac{\eta^{\text{clay}}}{\eta^{\text{clay}} + \varphi^{\text{clay}}}$ and $\varphi_n^{\text{clay}} = \frac{\varphi^{\text{clay}}}{\eta^{\text{clay}} + \varphi^{\text{clay}}}$. Finally, for the purpose of computing the effective elasticity of porous silt inclusion, one can define $f_n^r = \frac{f^r}{f^{\text{quartz}} + f^{\text{calcite}}}$ (r=quartz, calcite). Lastly, in a separate step to account for porosity in the inclusion phase, we define: $f_n^{\text{inc}} = \frac{f^{\text{inc}}}{f^{\text{inc}} + \phi^{\text{inc}}}$ and $\phi_n^{\text{inc}} = \frac{\phi^{\text{inc}}}{f^{\text{inc}} + \phi^{\text{inc}}}$.

4.3. Level I: effective elasticity

4.3.1. Immature system

The effective stiffness of the porous composite at level I of the model for immature organic-rich shale can be obtained by invoking Eqs. (1) and (2) as follows:

$$\mathbb{C}_{\text{I}}^{\text{hom}} = \langle \mathbb{C}^r : \mathbb{A}^r \rangle_{\Omega_{\text{I}}} \tag{17}$$

where $\Omega_{\text{I}} = \Omega_{\text{pc}} \cup \Omega_{\text{kerogen}}$ and $\Omega_{\text{pc}} = \Omega_{\text{clay}} \cup \Omega_{\varphi}$. The stiffness of porous clay can be computed using: $\mathbb{C}_{\text{pc}} = \langle \mathbb{C}^r : \mathbb{A}^r \rangle_{\Omega_{\text{pc}}}$. All the relevant volume fractions are defined in Section 4.2.1. The exact expression for strain localization tensor, Eq. (2), depends on the homogenization scheme used. Thus, in a Mori–Tanaka scheme for immature organic-rich shales, $\mathbb{C}^0$ in Eq. (2) should be replaced with $\mathbb{C}^{\text{kerogen}}$ when implementing Eq. (17). Additionally, estimation of $\mathbb{C}_{\text{pc}}$ requires replacing $\mathbb{C}^0$ with $\mathbb{C}^{\text{clay}}$ in Eq. (2).

4.3.2. Mature system

Similar to the case of immature organic-rich shale model, the expression for effective stiffness at level I of the mature model, $\mathbb{C}_{\text{I}}^{\text{hom}}$, looks exactly like Eq. (17) however with a different porosity distribution in the organic and inorganic phases in addition to a granular microtexture. These differences need to be considered when estimating $\mathbb{C}_{\text{I}}^{\text{hom}}$, $\mathbb{C}_{\text{pc}}$ and $\mathbb{C}_{\text{pk}}$. The relevant volume fractions are defined in Section 4.2.2.

4.4. Level II: effective elasticity

4.4.1. Immature system

The *rev* defined for the level II of the model includes two domains: the porous composite upscaled from level I and denoted by $\Omega_{\text{I}} = (1 - f^{\text{inc}})\Omega_{\text{II}}$ as well as the inclusion domain, $\Omega_{\text{inc}} = f^{\text{inc}}\Omega_{\text{II}}$. Similar to Eq. (17), the expression for estimating the effective drained stiffness at level II reads:

$$\mathbb{C}_{\text{II}}^{\text{hom}} = \langle \mathbb{C}^r : \mathbb{A}^r \rangle_{\Omega_{\text{II}}} \tag{18}$$

In a Mori–Tanaka homogenization scheme, when implementing Eq. (18), $\mathbb{C}^0$ in Eq. (2) should be replaced with $\mathbb{C}_{\text{I}}^{\text{hom}}$. Furthermore, $\mathbb{C}^{\text{inc}} = 3K^{\text{inc}}\mathbb{J} + 2G^{\text{inc}}\mathbb{K}$ with $\mathbb{J} = \frac{1}{3}(\delta_{ij}\delta_{kl})$ and $\mathbb{K} = \mathbb{I} - \mathbb{J}$. K^{inc} and G^{inc} were obtained by homogenizing bulk and shear moduli of pyrite ($K^{\text{pyrite}} = 138.9$ GPa, $G^{\text{pyrite}} = 112.3$ GPa) and quartz ($K^{\text{quartz}} = 37.9$ GPa, $G^{\text{quartz}} = 44.3$ GPa) (Mavko et al., 2003).

4.4.2. Mature system

For the macroscopic response of the mature system, one needs to account for the effective behavior of two porous systems; with a uniform pore pressure field prevailing inside them. Additionally, the effect of weakened interfaces between silt inclusion grains and the matrix needs to be considered. This can be done by replacing $\mathbb{P}$ in (2) with (6). The expression for $\mathbb{C}_{\text{II}}^{\text{hom}}$ is the same as (19) though the defined *rev* includes porous inclusions with its matrix elasticity obtained from homogenizing quartz and calcite ($K^{\text{calcite}} = 58.2$ GPa, $G^{\text{calcite}} = 28.3$ GPa) (Mavko et al., 2003) in a self-consistent manner.

4.5. Poroelastic coefficients and poroelasticity

The poroelastic response of a porous composite can be obtained by superimposing the solution to two boundary value problems. One involves the response of the system when an eigenstress, $\boldsymbol{\sigma}^T$, is imposed in the pore space, while keeping a zero displacement boundary condition. The other accounts for the response of the system when a displacement boundary condition is imposed. The application of Hill Lemma and Levin's theorem enables one to obtain and to upscale the Biot solid modulus, N, and Biot tensor of pore pressure coefficients, $\boldsymbol{\alpha}$. With these at hand, assuming full saturation, one can obtain the

Table 2
Poroelastic coefficients for the immature system for each defined *rev*.

Ω_{pc}	$\boldsymbol{\alpha}_{\mathrm{pc}} = \varphi_n \mathbf{1}: \mathbb{A}^{\varphi n}$ $\dfrac{1}{N_{\mathrm{pc}}} = \mathbf{1}: \mathbb{S}^{\mathrm{clay}}: (\boldsymbol{\alpha}_{\mathrm{pc}} - \varphi_n \mathbf{1})$
Ω_I	$\boldsymbol{\alpha}_{\mathrm{I}} = \varphi \mathbf{1}: \mathbb{A}^{\varphi}$ $\dfrac{1}{N_{\mathrm{I}}} = \dfrac{1 - \eta^{\mathrm{kerogen}}}{N_{\mathrm{pc}}} + \boldsymbol{\alpha}_{\mathrm{pc}}: (\mathbb{C}^{pc} - \mathbb{C}^{\mathrm{kerogen}})^{-1}: (-\boldsymbol{\alpha}_{\mathrm{I}} + (1 - \eta^{\mathrm{kerogen}})\boldsymbol{\alpha}_{\mathrm{pc}})$
Ω_{II}	$\boldsymbol{\alpha}_{\mathrm{II}} = \boldsymbol{\alpha}_{\mathrm{I}}: (\mathbb{I} - f^{\mathrm{inc}} \mathbb{A}^{\mathrm{inc}})$ $\dfrac{1}{N_{\mathrm{II}}} = \dfrac{1 - f^{\mathrm{inc}}}{N_{\mathrm{I}}} + \boldsymbol{\alpha}_{\mathrm{I}}: (\mathbb{C}_{\mathrm{I}}^{\mathrm{hom}} - \mathbb{C}^{\mathrm{inc}})^{-1}: (-\boldsymbol{\alpha}_{\mathrm{II}} + (1 - f^{\mathrm{inc}})\boldsymbol{\alpha}_{\mathrm{I}})$

undrained behavior of a porous composite as follows (Dormieux et al., 2006):

$$\mathbb{C}_{\mathrm{un}}^{\mathrm{hom}} = \mathbb{C}^{\mathrm{hom}} + (M\boldsymbol{\alpha} \otimes \boldsymbol{\alpha}) \tag{19}$$

$$\frac{1}{M} = \frac{1}{N} + \frac{\phi}{K^f} \tag{20}$$

The saturating fluid was assumed to be water with a bulk modulus, K^f of 2.3 GPa. The final expressions for poroelastic coefficients are summarized in Table 2 for the immature system and Table 3 for the mature one.

5. Results

5.1. Calibration procedure

The calibration of the model was performed by downscaling the macroscopic elasticity of both Woodford (immature) and Haynesville (mature) data sets by minimizing the Frobenius norm of the measured values and the predicted undrained elasticity, $\mathbb{C}_{\mathrm{II,un}}^{\mathrm{hom}}$; as mathematically summarized in Eq. (21). The degrees of freedom associated with this multi-objective minimization problem are outlined in Eq. (22). The silt inclusion grain radius for weakened interface model was estimated from a SEM image on Haynesville sample (see Fig. 3). The transversely isotropic clay elasticity, $\mathbb{C}^{\mathrm{clay}}$, was constrained to

Table 3
Poroelastic coefficients for the mature system for each defined *rev*.

Ω_{pk}	$\alpha_{\mathrm{pk}} = 1 - \dfrac{K_{\mathrm{pk}}}{K^{\mathrm{kerogen}}}$ $\dfrac{1}{N_{\mathrm{pk}}} = \dfrac{\alpha_{\mathrm{pk}} - \varphi_n^{\mathrm{kerogen}}}{K^{\mathrm{kerogen}}}$
Ω_{pc}	$\boldsymbol{\alpha}_{\mathrm{pc}} = \varphi_n \mathbf{1}: \mathbb{A}^{\varphi_n^{\mathrm{clay}}}$ $\dfrac{1}{N_{\mathrm{pc}}} = \mathbf{1}: \mathbb{S}^{\mathrm{clay}}: (\boldsymbol{\alpha}_{\mathrm{pc}} - \varphi_n^{\mathrm{clay}} \mathbf{1})$
Ω_{I}	$\boldsymbol{\alpha}_{\mathrm{I}} = (\varphi^{\mathrm{clay}} + \eta^{\mathrm{clay}})\boldsymbol{\alpha}_{\mathrm{pc}} + (\varphi^{\mathrm{kerogen}} + \eta^{\mathrm{kerogen}})\boldsymbol{\alpha}_{\mathrm{pk}}$ $\dfrac{1}{N_{\mathrm{I}}} = (\varphi^{\mathrm{clay}} + \eta^{\mathrm{clay}})\dfrac{1}{N_{\mathrm{pc}}} + (\varphi^{\mathrm{kerogen}} + \eta^{\mathrm{kerogen}})\dfrac{1}{N_{\mathrm{pk}}}$
Ω_{pinc}	$\alpha_{\mathrm{pinc}} = 1 - \dfrac{K_{\mathrm{pinc}}}{K^{\mathrm{inc}}}$ $\dfrac{1}{N_{\mathrm{pinc}}} = \dfrac{\alpha_{\mathrm{pinc}} - \varphi_n^{\mathrm{inc}}}{K^{\mathrm{inc}}}$
$\Omega_{\mathrm{I}}^{\mathrm{up.}}$	$\boldsymbol{\alpha}_{\mathrm{I}}^{\mathrm{up.}} = \boldsymbol{\alpha}^{I}: (\mathbb{I} - f^{\mathrm{pinc}} \mathbb{A}^{\mathrm{pinc}})$ $\dfrac{1}{N_{\mathrm{I}}^{\mathrm{up.}}} = \dfrac{1 - f^{\mathrm{pinc}}}{N_{\mathrm{I}}^{\mathrm{up.}}} + \boldsymbol{\alpha}_{\mathrm{I}}^{\mathrm{up.}}: (\mathbb{C}_{\mathrm{I}}^{\mathrm{hom}} - \mathbb{C}_{\mathrm{pinc}})^{-1}: (-\boldsymbol{\alpha}_{\mathrm{I}}^{\mathrm{up.}} + (1 - f^{\mathrm{pinc}})\boldsymbol{\alpha}_{\mathrm{I}}^{\mathrm{up.}})$
Ω_{II}	$\boldsymbol{\alpha}_{\mathrm{II}} = f^{\mathrm{pinc}}\boldsymbol{\alpha}_{\mathrm{pinc}} + (1 - f^{\mathrm{pinc}})\alpha_{\mathrm{I}}^{\mathrm{up.}}$ $\dfrac{1}{N_{\mathrm{II}}} = f^{\mathrm{pinc}}\dfrac{1}{N_{\mathrm{pinc}}} + (1 - f^{\mathrm{pinc}})\dfrac{1}{N_{\mathrm{I}}^{\mathrm{up.}}}$

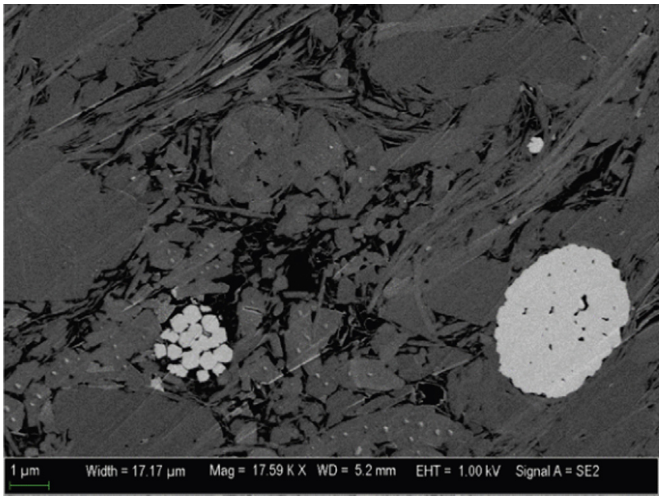

Fig. 3. A Scanning Electron Microscope (SEM) image on Haynesville sample. An average inclusion grain radius of 2 μm, input for imperfect interface model, was chosen. This image is courtesy of Amer Deirieh.

ensure its positive definiteness. Furthermore, kerogen bulk modulus, K^{kerogen}, was introduced as the sole degree of freedom associated with kerogen. This is justified from the results of Bousige et al. (2015) which suggest $\nu^{\text{kerogen}} \approx 0.25$, independent of ρ^{kerogen} or its state of maturity. This is done utilizing the functional relationship, as displayed in Fig. 6, to constrain density and bulk modulus variable spaces – based on maturity. This allows us to avoid any assumptions *a priori* regarding elasticity, density and consequently volume fraction of the kerogen phase. For the mature system we used simulation results of Bousige et al. (2015) on re-constructed Marcellus kerogen (MAR) with a vitrinite reflectance of $\%R_0 = 2.2$; while for the immature one, we utilized the reported values of Bousige et al. (2015) on Middle East Kerogen (MEK) with a vitrinite reflectance of $\%R_0 = 0.55$:

$$\min_{\underline{d}} \left(\sum_{\text{Woodford}} \| \left(\mathbb{C}^{\text{hom}}_{\text{II,un}}\right)^{\text{immature}} - \mathbb{C}^{\text{macro}}_{\text{Woodford}} \|_F + \sum_{\text{Haynesville}} \| \left(\mathbb{C}^{\text{hom}}_{\text{II,un}}\right)^{\text{mature}} - \mathbb{C}^{\text{macro}}_{\text{Haynesville}} \|_F \right) \tag{21}$$

where $\|\cdots\|_F$ denotes Frobenius norm and

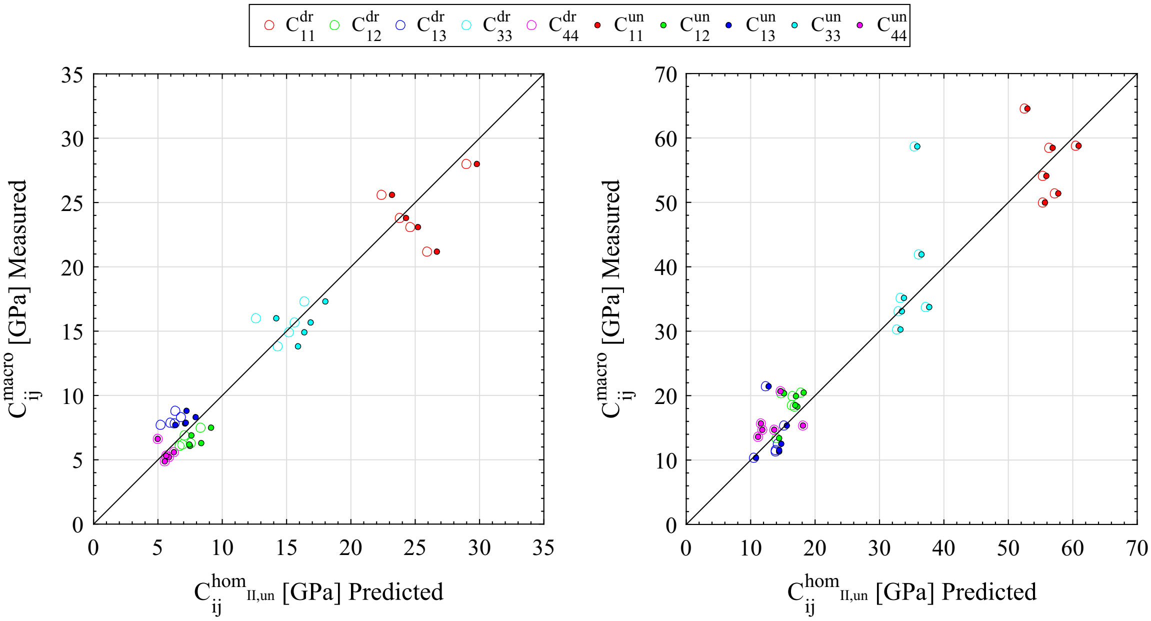

Fig. 4. Calibration quality check by comparing predicted macroscopic values (drained and undrained) for Woodford on the left and Haynesville on the right against the measured values.

Table 4
Available reported anisotropic clay elasticity obtained from a combination of experimental (laboratory/simulation) techniques.

Clay type	C_{11} (GPa)	C_{12} (GPa)	C_{13} (GPa)	C_{33} (GPa)	C_{44} (GPa)
Muscovite[a]	178	42.40	14.50	54.90	12.20
Muscovite[b]	184.30	48.30	23.80	59.10	16
Kaolinite[c]	171.50	38.90	26.90	52.60	14.80
Muscovite[d]	250	60	35	80	35
Chlorite[c]	181.80	56.80	90.10	96.80	11.40
Illite (ReaxFF)[e]	216 ± 5	76 ± 9	29 ± 4	93 ± 1	10.8 ± 0.4
Illite (ClayFF)[e]	292.5 ± 0.5	128.3 ± 0.4	16.67 ± 0.08	48.9 ± 0.1	9.82 ± 0.04

[a] Aleksandrov and Ryzhova (1961).
[b] Vaughan and Guggenheim (1986).
[c] Katahara (1996).
[d] Seo et al. (1999).
[e] Hantal et al. (2014).

$$\underline{d} = \langle C_{11}^{\text{clay}}, C_{12}^{\text{clay}}, C_{13}^{\text{clay}}, C_{33}^{\text{clay}}, C_{44}^{\text{clay}}, K_{\text{Woodford}}^{\text{kerogen}}, K_{\text{Haynesville}}^{\text{kerogen}}, \alpha, \beta\rangle \tag{22}$$

5.2. Calibration and validation results

Calibration results can be summarized as follows: $C_{11}^{\text{clay}} = 103.0$ GPa, $C_{12}^{\text{clay}} = 41.6$ GPa, $C_{13}^{\text{clay}} = 34.1$ GPa, $C_{33}^{\text{clay}} = 43.3$ GPa, $C_{44}^{\text{clay}} = 7.7$ GPa, $K_{\text{Woodford}}^{\text{kerogen}} = 4.2$ GPa, $K_{\text{Haynesville}}^{\text{kerogen}} = 1.4$ GPa, $\alpha = 1.53 \times 10^{-7}$ GPa^{-1}, and $\beta = 1.17\times^{-7}$ GPa^{-1}. As a quality check, the measured values are plotted against predictions using the calibrated results, displayed in Fig. 4. The grain scale indentation moduli of clay were calculated, using (Delafargue and Ulm, 2013):

$$m_3 = 2\sqrt{\frac{C_{11}C_{33} - C_{13}^2}{C_{11}}\left(\frac{1}{C_{44}} + \frac{2}{\sqrt{C_{11}C_{33}} + C_{13}}\right)^{-1}} \tag{23}$$

$$m_1 \approx \sqrt{\sqrt{\frac{C_{11}}{C_{33}}}\frac{C_{11}^2 - C_{12}^2}{C_{11}}M_3} \tag{24}$$

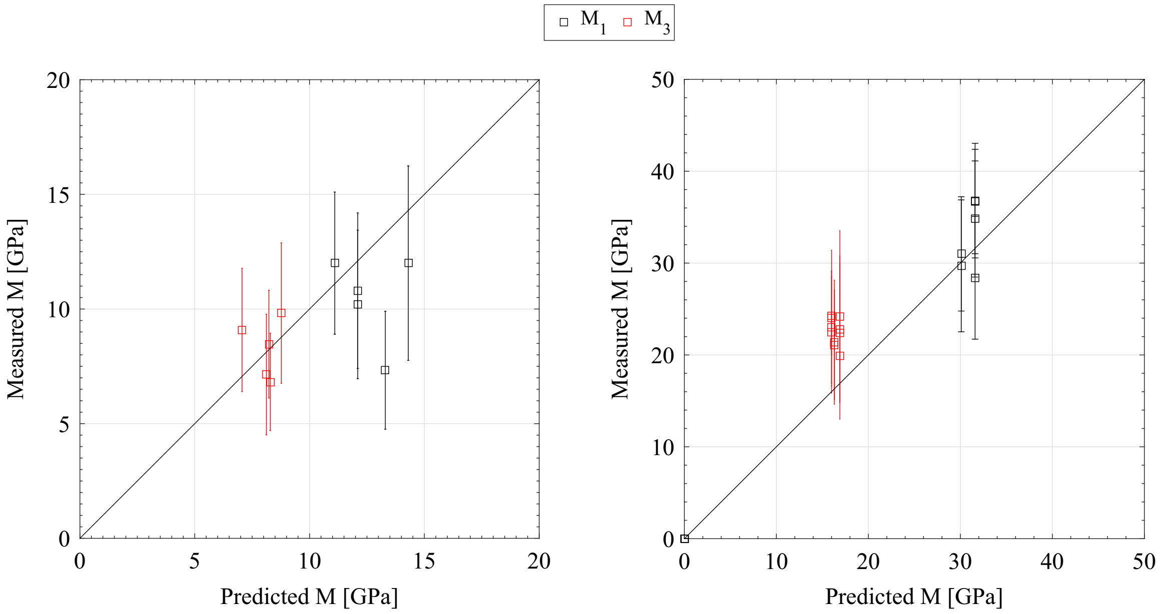

Fig. 5. Validation by means of nanoindentation for Woodford on the left and Haynesville on the right against the measured values.

Table 5
Means and standard deviations of relative error between measured and predicted indentation moduli (level I). For Haynesville data, same sample size for the reported measurements is assumed.

Indentation moduli	Immature system		Mature system	
	$\bar{e}$	e_σ	$\bar{e}$	e_σ
M_1	0.36	0.35	−0.03	0.50
M_3	0.05	0.21	−0.58	0.55

We obtain $m_1 = 62.3$ GPa and $m_3 = 29.2$ GPa, in x_1 and x_3 directions, respectively. A number of published transversely isotropic clay elastic values are reported in Table 4 and agree well with our results. For further validation, the predicted indentation moduli at level I of the model are compared to the measured values on Woodford and Haynesville samples. The results are displayed in Fig. 5. The quality of this validation step is quantified using the mean, $\bar{e}$, and the standard deviation, e_σ, of relative error, e_i; computed as follows (Hellmich and Ulm, 2005): $e_i = \frac{(X_i - Y_i)}{Y_i}$; $\bar{e} = \frac{1}{n}\sum e_i$ and $e_\sigma = \sqrt{\frac{1}{n-1}\sum (e_i - \bar{e})^2}$; where X_i and Y_i represent model predictions and measurements, respectively and n represents the number of samples in the data set. The calculated $\bar{e}$ and e_σ are reported in Table 5. The obtained values for compliances are consistent with derivation of imperfect interface model by Qu (1993a,b) for small compliances, hence slightly weakened interfaces. Additionally, the order of magnitude for α and β compares well with reported normal and tangential compliances of a crack complied by Prioul et al. (2007).

5.3. Application: kerogen density and microporosity estimations

The unique approach in accounting for microtextural transition of source rocks with maturity via a mean field theory enriched with data from molecular simulations enables us to indirectly access microtextural information from elastic measurements. An important parameter for exploration geophysicists is kerogen density, ρ^{kerogen}. This density reflects the degree of maturity of the organics and it carries information pertaining to its microporosity, φ^{micro}. Having access to φ^{micro} from elastic based field measurements such as seismic or sonic wave velocities can revolutionize the current reserves estimation techniques.

We estimated kerogen's bulk modulus and consequently its density utilizing indentation data on both mature (Marcellus, Fayetteville) and immature (Barnett, Antrim) formations (see Appendix B) via:

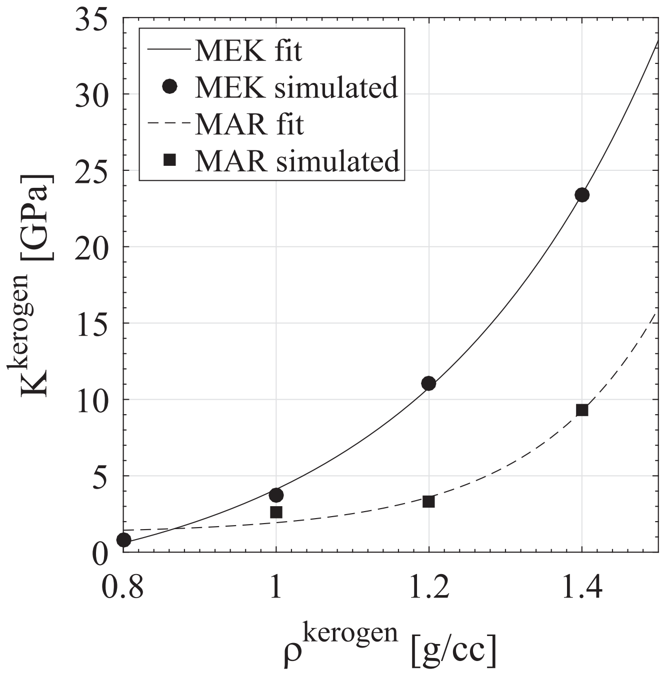

Fig. 6. Bulk modulus of kerogen against density for two of the samples studied by Bousige et al. (2015) using a Molecular Dynamics (MD) Hybrid Reverse Monte-Carlo simulation (HRMC) method. MAR refers to a mature kerogen extracted from a sample of Marcellus shale and MEK is the kerogen extracted from an organic-rich shale sample from the Middle East, classified as immature kerogen. The fit is a power-law of the form $y = a + be^{cx}$ with $a^{\text{MAR}} = 1.2278$, $b^{\text{MAR}} = 0.0016$, $c^{\text{MAR}} = 6.0783$, $a^{\text{MEK}} = -3.2886$, $b^{\text{MEK}} = 0.2997$ and $c^{\text{MEK}} = 3.2070$.

Table 6
Estimated kerogen density and microporosity of kerogen from elasticity.

Estimations from elasticity	C1	D1	F1	F2	F3	F4	F5	G1
K^{kerogen} (GPa)	4.1	6.4	35.0	35.0	9.0	6.1	7.7	5.2
ρ^{kerogen} (g/cc)	1.0	1.1	1.6	1.6	1.4	1.3	1.4	1.3
φ^{micro} (%)	56	52	28	28	38	42	40	43

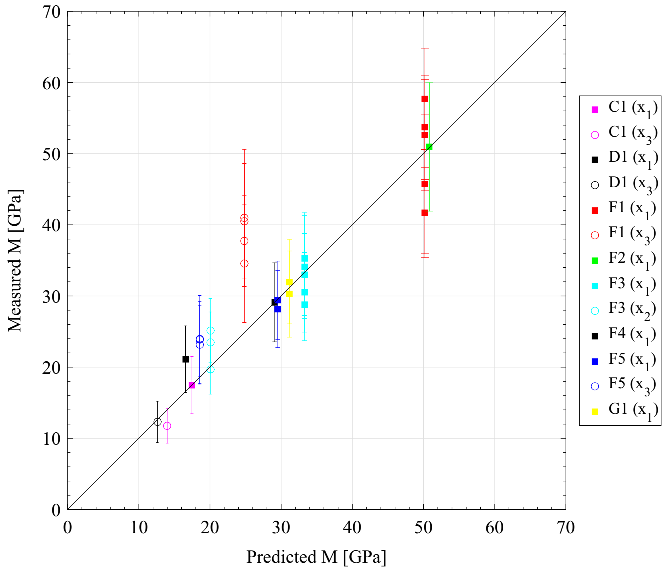

Fig. 7. Application of the outlined methodology to estimate kerogen density. The predicted values reflect model's prediction after using the estimated kerogen bulk modulus obtained by downscaling nanoindentation data.

$$\min_{K^{\text{kerogen}}}\left(\sum_{\text{formation}} \| M^{\text{predicted}} - M^{\text{measured}} \|_F\right) \tag{25}$$

Then, assuming a graphite based organic backbone with a density, $\rho_g^{\text{kerogen}} = 2.26$ g/cc (Pierson, 1993); we can estimate φ^{micro} via: $\rho^{\text{kerogen}} = (1 - \varphi^{\text{micro}})\rho_g^{\text{kerogen}}$. The results are reported in Table 6 and the quality of the fit is displayed in Fig. 7. The predicted kerogen densities are consistent with our expectations of higher values for mature systems. The high values for kerogen bulk modulus for F1 and F2 are a consequence of low TOC for these two samples (0.5 and 1 by mass %, respectively). This confirms our hypothesis of capturing the first-order contribution of organic maturity on effective elasticity as a texture effect. For example, for the case of F1, the measured indentation moduli, $M_1 = 50.3$ GPa and $M_3 = 38.4$ GPa, agree well with predictions using a vanishing kerogen stiffness, $M_1 = 46.1$ GPa and $M_3 = 22.4$ GPa; not that different compared to predictions using a kerogen bulk modulus of 35 GPa: $M_1 = 50.2$ GPa and $M_3 = 24.8$ GPa. Furthermore, utilizing available data for Hydrogen Index (HI) of kerogen in the studied samples, a linear relationship between kerogen density and HI is established, as displayed in Fig. 8. Additional data points on this plot, combined with other maturity indicators such as e.g. vitrinite reflectance, sp^2/sp^3 ratio (Bousige et al., 2015) and normalizing these variable spaces by the values for a material representing the upper end of maturity (e.g. pyrobitumen, graphite); would provide an indirect technique to relate kerogen density to the degree of maturity.

6. Sensitivity analysis

A comprehensive sensitivity analysis of the model by means of Spearman's partial Rank Correlation Coefficient (SPRCC) (Gibbons and Chakraborti, 2003) is presented to assess the sensitivity of the normalized variance of the model output with regard to uncertainty associated with each input parameter. Specifically, the sensitivity of the undrained macroscopic elasticity, the anisotropy parameters (Thomsen, 1986) and the minimum *in situ* horizontal stress to variations in model input;namely $\mathbb{C}^{\text{clay}}$, ϕ, K^{kerogen}, organic content (TOC), and fluid bulk modulus, K^f, are studied. Additionally, for the mature

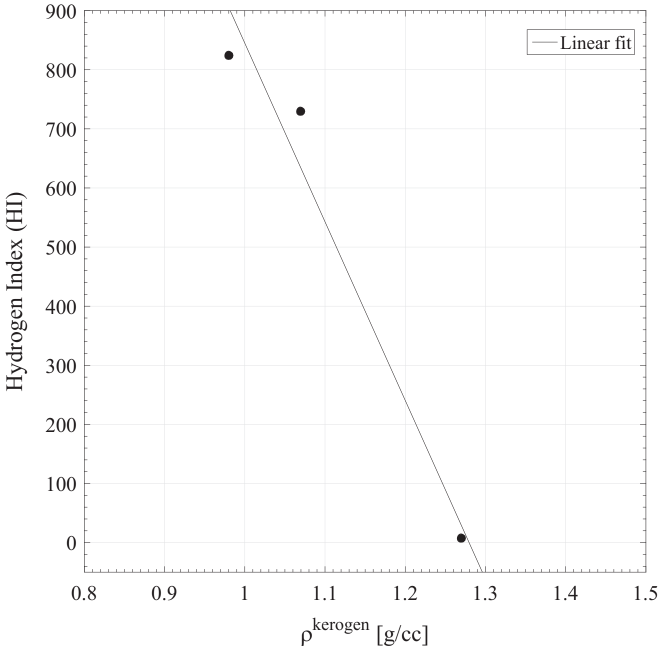

Fig. 8. The fit between Hydrogen Index (HI) and kerogen density is in a linear form: $y = ax + b$, where $a = -3022.2$, b=3867.2 and $R^2 = 0.96$. Other maturity indicator such as $\%R_0$, sp^2/sp^3, and Oxygen Index can be used to establish such relationship that are useful for the assessment of the degree of maturity of kerogen from elasticity.

model, the sensitivity of output to tangential, α, and normal, β, interface compliances as well as silt inclusion grain radius (radius or 'a') is explored. The Thomsen parameters are defined as (Thomsen, 1986): $\epsilon = \frac{C_{11} - C_{33}}{2C_{33}}$, $\gamma = \frac{C_{66} - C_{44}}{2C_{44}}$ and $\delta * = \frac{1}{2C_{33}^2}[2(C_{13} + C_{44})^2 - (C_{33} - C_{44})(C_{11} + C_{33} - 2C_{44})]$. The solution for the minimum *in situ* horizontal stress in a transversely isotropic formation reads (Thiercelin and Plumb, 1994): $\sigma_h = \frac{C_{13}}{C_{33}}(\sigma_3 - \alpha_3 P_p) + \alpha_1 P_p + (C_{11} - \frac{C_{13}^2}{C_{33}})\varepsilon_2 + (C_{12} - \frac{C_{13}^2}{C_{33}})\varepsilon_1$; where P_p denotes pore pressure and $\varepsilon_{1,2}$ represents tectonically induced strains (assumed to be zero). To perform the sensitivity analysis, each input parameter was introduced stochastically with a normal distribution, as follows:

$$X \sim N(\mu, \sigma) \tag{26}$$

N denotes a normal distribution. μ and σ represent the mean and standard deviation needed to characterize a normally distributed random variable, X. All distributions were defined using a coefficient of variation, $V = \frac{\sigma}{\mu} = 0.10$. The stochastic inputs are summarized in Table 7. The analysis was performed by means of 1500 Monte Carlo simulations ensuring the convergence of the result. The results are displayed in Fig. 10 for the mature system and in Fig. 9 for the immature case.

Table 7
Stochastically defined input for Spearman's partial rank correlation coefficient analysis by means of 1500 Monte Carlo simulations.

Input parameters	Distribution types	μ	σ	V
C_{11}^{clay} (GPa)	Normal	103.0	10.3	0.1
C_{12}^{clay} (GPa)	Normal	41.6	4.2	0.1
C_{13}^{clay} (GPa)	Normal	34.12	3.4	0.1
C_{33}^{clay} (GPa)	Normal	43.3	4.3	0.1
C_{44}^{clay} (GPa)	Normal	7.7	0.77	0.1
ϕ (%)	Normal	13	1.3	0.1
TOC (mass%)	Normal	15.7	1.57	0.1
$K^{kerogen}$ (GPa)	Normal	1.69	0.16	0.1
α (GPa)$^{-1}$	Normal	1.53×10^{-7}	1.53×10^{-8}	0.1
β (GPa)$^{-1}$	Normal	1.17×10^{-7}	1.17×10^{-8}	0.1
Radius (a) (m)	Normal	2×10^{-6}	4×10^{-7}	0.1

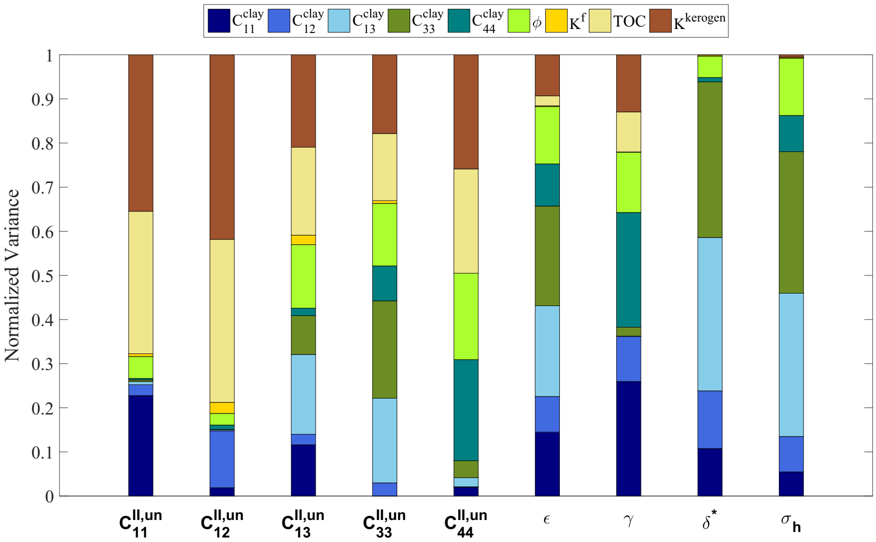

Fig. 9. SPRCC results immature organic-rich shale model.

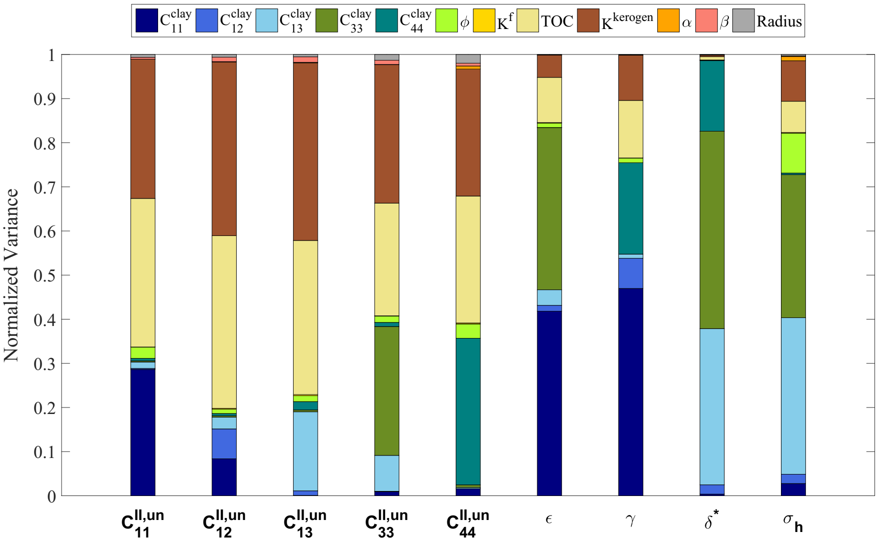

Fig. 10. SPRCC results for mature organic-rich shale model.

The SPRCC analyses for the immature model suggest that TOC, and $K^{kerogen}$ are the most influential parameters on the effective undrained macroscopic elasticity while for Thomsen parameters and σ_h clay elasticity, $\mathbb{C}^{clay}$, seems to play the dominant role. Same trends can be observed for the mature model. Furthermore, the parameters associated with weakened interface model, namely tangential and normal interface compliance, α and β, respectively, as well as silt inclusion grain radius have negligible contribution to the normalized variance of the output.

7. Discussions

The combination of micro-textural transition of organic-rich shale with maturity and the results of maturity dependent molecular studies on kerogen led us to a set of elastic values in relatively good agreement with published transversely isotropic results (see Table 4), hinting at the existence of an effective set of illite-rich clay elasticity for similar depositional environments. The model presented captures asymptotic cases for organic maturity. To model intermediate maturity levels, one would need tools beyond mean field theory in order to incorporate higher order statistical distribution of microtextural parameters, i.e. beyond volume fraction information. The porous silt inclusions for the case of mature model arises as a consequence of a self-consistently distributed porosity in all solid phases. This is a first-order approach to distinguish porosity distribution in mature vs. immature systems. Further quantitative lab characterization with regard to porosity distribution in various phases can be easily incorporated into the model once available. Lastly, a larger data sets for calibration would result in improved values, though the framework established remains rigorous.

Furthermore, the contribution of burial and diagenetic processes on the evolution of organic matter and on overall elasticity of organic-rich shales is captured by introducing slightly weakened interfaces. In reality, organic-rich shale deposits, over geological time, not only go through burial; but also uplifting and erosion, entailing a $\Delta\theta < 0$. In addition, the geothermal gradient at the geological time and burial location become a critical factor in terms of kerogen maturation and its effect on overall poroelastic behavior of organic-rich shales. Kerogen maturation is a complex function of exposure time, pressure, temperature and composition that is going over rapid physical and chemical changes (in geological time scale) as it generates hydrocarbons. Some may argue that any discontinuities created in the subsurface such as micro-cracks and weakened interfaces would re-cement over geological times and thus should not be considered in a modeling framework. However, one needs to be aware that organic-rich shales are more intricate than other sedimentary rocks due to the presence of both organics and inorganics. Both cementation and maturation occur over geological time scales, though the kinetics involved in these processes and the characteristic time scale associated with them are not well understood. Chances are that these processes occur on time scales that are orders of magnitude apart – though still within the same geological time scale. It is also important to recognize that inorganics, e.g. quartz, for the most part remain physically, chemically and structurally inert when exposed to pressure and temperature, in the range relative to subsurface exploration (Sorrell et al., 1974). On the other hand, kerogen seems to go through chemical, physical and structural changes – and possibly a glass transition – during maturation. A parameter that we identified in our rationalization was the coefficient of linear thermal expansion, α_{Th}. For inorganics such as quartz, α_{Th} seems to not change much over the temperature range of our interest (Sorrell et al., 1974), however, organics seem to be sensitive to the exposed temperature, pressure and more robustly, the maturation state; which partly addresses the existence of weakened interfaces.

With molecular simulation results at the heart of our model, we are able to link kerogen maturity, elasticity and density rigorously, promising a new horizon in subsurface characterization using elastic based measurements. The choice of a $\nu^{\mathrm{kerogen}} = 0.25$ is based on the result of molecular simulations which itself follows fundamental principles of physics.

8. Conclusions

Merging molecular results with continuum micromechanics in the form of constraining variable spaces promise to be a powerful tool for capturing intricate elastic and poroelastic behavior of organic/inorganic porous composites. Our original multi-scale modeling approach utilizes a mean field theory to account for asymptotic textural transition of organic-rich shales with maturity. The homogenization schemes employed, namely: Mori–Tanaka and self-consistent techniques implicitly provide insights into phase interactions and force transmission in these composites as their texture evolve from a matrix/inclusion into a granular one with burial and diagenetic processes taking place over geological time scale. The obtained elastic values for illite-rich clays compare well with reported values obtained with different techniques performed at different scales. Having microporous kerogen at the heart of our model enable us to indirectly access information such as kerogen's density and its microporosity with profound implications on reserves estimation from elastic measurements. Finally, we have utilized Spearman's partial rank correlation coefficient for a comprehensive sensitivity analysis for our model and introduced it as a tool for geoscientists to improve confidence in their computations.

Acknowledgment

This work was funded by X-Shale Hub: the Science and Engineering of Gas Shale, a collaboration between Shell, Schlumberger, and the Massachusetts Institute of Technology. The authors would like to acknowledge Dr. Ronny Hofmann of Shell for providing data for macroscopic elastic characterization of Haynesville samples. Thanks to Amer Deirieh for providing SEM image of Haynesville shale and Dr. Colin Bousige for schematics of molecular structure of kerogen.

Appendix A. Calibration and validation data sets

Table A1
Elasticity, mineralogy, organic content and porosity of Woodford (Abousleiman et al., 2007) and Haynesville samples used in calibration of the model.

Measured quantities	A1	A2	A3	A4	A5	B1	B2	B3	B4	B5	B6
Quartz (mass%)	37	31	33	34	27	30	27	16	20	32	28
Feldspar (mass%)	2	–	2	2	2	7	9	5	6	11	10
Plagioclase (mass%)	3	3	3	3	3	–	–	–	–	–	–
Carbonate (mass%)	0.5	3	1	–	6	30	22	65	51	9	12
Ankerite (mass%)	2	4	2	7	8	–	–	–	–	–	–
Pyrite (mass%)	9	13	10	6	3	–	–	–	–	–	–
Clay (mass%)	30	28	31	36	36	30	38	11	20	43	38
Kerogen (mass%)	17	17.5	18	12	14	2.48	3.34	1.57	2.65	3.30	3.16
ϕ (%)	16	21	16	19	21	6.64	7.36	4.61	5.57	7.16	7.59
C_{11}^{macro} (GPa)	23.1	25.6	23.8	28	21.2	58.7	54.1	49.9	64.6	51.4	58.52
C_{12}^{macro} (GPa)	15.7	16	14.9	17.3	13.8	20.5	19.9	13.4	20.3	18.3	18.5
C_{13}^{macro} (GPa)	5.2	6.6	5.3	5.6	4.9	15.4	11.3	10.4	21.4	12.6	11.6
C_{33}^{macro} (GPa)	8.8	7.7	7.8	8.3	7.9	33.8	33.1	41.9	58.7	30.3	35.1
C_{44}^{macro} (GPa)	6.9	6.1	6.2	7.5	6.3	14.9	15.7	15.3	20.7	13.6	14.6

Table A2
Measured Woodford (Bobko, 2008) and Haynesville (Abedi et al., 2015) indentation moduli used for validation.

Samples	M_1 (GPa)	M_3 (GPa)
A1	10.79 ± 3.39	8.47 ± 2.35
A2	11.95 ± 3.1	9.09 ± 2.69
A3	10.24 ± 3.24	6.82 ± 2.12
A4	11.98 ± 4.24	9.82 ± 3.06
A5	7.33 ± 2.57	7.14 ± 2.63
B1	–	–
		23.04 ± 6.07
B2	–	22.51 ± 6.64
		24.26 ± 4.19
		24 ± 7.4
B3	–	–
B4	–	–
	36.83 ± 6.24	
B5	36.68 ± 5.68	22.84 ± 7.99
	28.39 ± 6.68	24.22 ± 9.33
	34.8 ± 6.32	22.36 ± 7.52
		19.85 ± 6.88
B6	29.68 ± 7.18	21.09 ± 5.94
	30.98 ± 6.22	21.41 ± 6.75

Appendix B. Application data set

Table B1
Mineralogy, kerogen content, porosity and HI of samples used in application of the model for estimating kerogen microporosity.

Measured quantities	C1	D1	F1	F2	F3	F4	F5	G1
Quartz (mass%)	29.7	40.9	19.7	18.7	29.6	29.4	36.2	28.8
Clay (mass%)	41.8	31.4	29.2	29.3	38.4	32.2	32.2	25.1
Albite (mass%)	2.2	3.5	–	–	–	–	–	6.3
Calcite (mass%)	2.6	–	30.6	3.3	3.1	13.3	3	22.8
Microline (mass%)	3.2	–	–	–	–	–	–	–
Pyrite (mass%)	0.5	3.1	1.5	1.8	8.7	7.3	11.7	2.5
Gypsum (mass%)	7.8	–	–	–	–	–	–	–
Dolomite (mass%)	–	4.4	4.4	3.6	1.4	2.4	1.5	8.9
Sanidine (mass%)	–	7.9	–	–	–	–	–	–
Plagioclase (mass%)	–	–	3.2	3.5	6.0	4.8	5.6	–
Siderite (mass%)	–	–	0.5	0.7	0.7	0.4	0.3	–
Anatase (mass%)	–	–	0.2	0.1	0.4	0.4	0.5	
Barite (mass%)	–	–	–	–	1.5	–	–	–
Muscovite (mass%)	–	–	10.7	9.6	10.2	10.0	9.0	–
Kerogen (mass%)	12.2	9.6	0.5	1.0	7.7	7.3	8.2	4.92
ϕ (%)	7.3	8.8	8.4	7.9	7.2	5.2	6.5	4
Hydrogen Index (HI) [S2 × 100/TOC]	824	730	–	–	–	–	–	7

Table B2
Nanoindentation moduli used as an elastic measurement to estimate kerogen's microporosity (Abedi et al., 2015).

Samples	M_1 (GPa)	M_3 (GPa)
C1	17.37 ± 4.02	11.78 ± 2.45
D1	21.11 ± 4.68	12.31 ± 2.91
	45.74 ± 9.81	
	41.70 ± 6.32	34.59 ± 8.31
F1	53.37 ± 7.32	40.95 ± 9.61
	52.61 ± 7.83	37.74 ± 6.41
	57.70 ± 7.12	40.50 ± 8.11
	28.81 ± 5.04	
F2	50.94 ± 9.01	–
	35.30 ± 6.39	19.66 ± 3.44
F3	33.02 ± 5.59	25.17 ± 4.48
	34.06 ± 7.23	23.51 ± 4.24
F4	29.1 ± 5.55	–
		23.85 ± 6.22
F5	28.17 ± 5.39	23.92 ± 5.28
	29.41 ± 5.50	23.19 ± 5.51
G1	31.99 ± 5.91	–
	30.27 ± 6.05	

References

Abedi, S., Slim, M., Hofmann, R., Bryndzia, T., Ulm, F.-J., 2015. Nano-chemomechanical signature of organic-rich shales: a coupled indentation-edx analysis. Acta Geotech., submitted for publication.

Abousleiman, Y., Tran, M., Hoang, S., Bobko, C., Ortega, J., Ulm, F.-J., 2007. Geomechanics field and lab characterization of Woodford shale: The next gas play. In: Proceedings, Society of Petroleum Engineers Annual Technical Conference and Exhibition SPE 110120.

Ahmadov, R., 2011. Micro-textural, elastic and transport properties of source rocks. Doctor of philosophy. Stanford University.

Aleksandrov, K., Ryzhova, T., 1961. Elastic properties of rock-forming minerals. ii. Layered silicates. Bull. USSR. Acad. Sci. Geophys. Ser. 9, 1165–1168.

Bangham, D., Franklin, R., 1946. Thermal expansion of coals and carbonised coals. Proc. R. Soc. A 27, 147–160.

Beneviste, Y., 1987. A new approach to the application of Mori–Tanaka's theory in composite materials. Mech. Mater. 6, 147–157.

Bobko, C., 2008. Assessing the mechanical microstructure of shale by nanoindentation: the link between mineral composition and mechanical properties. Doctor of philosophy. Massachusetts Institute of Technology.

Bousige, C., Ghimbeu, C., Vix, C., Pomerantz, A., Suleimenova, A., Vaughan, G., Garbarino, G., Feygenson, M., Wildgruber, C., Ulm, F.-J., Pellenq, J.-M., Cosane, B., 2015. Realistic molecular model of mature and immature kerogens in organic-rich shales. Nat. Mater, in press.

Budiansky, B., 1965. On the elastic moduli of some heterogeneous materials. J. Mech. Phys. Solids 13 (4), 223–227.

Curtis, M., Sondergeld, C., Rai, C., 2013. Relationship between organic shale microstructure and hydrocarbon generation, SPE164540.

Delafargue, A., Ulm, F.-J., 2013. Explicit approximation of the indentation modulus of elasticity orthotropic solids for conical indenters. Int. J. Solids Struct. 41, 7351–7360.

Dormieux, L., Kondo, D., Ulm, F.-J., 2006. In: MicroporomechanicsWiley, Chichester.

Eshelby, J., 1957. The determination of the elastic field of an ellipsoidal inclusion, and related problems. Proc. R. Soc. A 241, 376–396.

Gibbons, J., Chakraborti, S., 2003. In: Nanoparametric Statistical InferenceMarcel Dekker, Inc., New York, USA.

Hantal, G., Brochard, L., Laubie, H., Ebrahimi, D., Pellenq, J.-M., Ulm, F.-J., Cosane, B., 2014. Atomic-scale modeling of elastic and failure properties of clays. Mol. Phys.: An Int. J. Interface Between Chem. Phys. 112, 1294–1305.

Hellmich, C., Ulm, F.-J., 2005. Drained and undrained poroelastic properties of healthy and pathological bone: a poro-micromechanical investigation. Transp. Porous Media 58 (February (3)), 243–268.

Hershey, A., 1954. The elasticity of an isotropic aggregate of anisotropic cubic crystals. J. Appl. Mech. 21, 226–240.

Hill, R., 1965. A self-consistent mechanics of composite materials. J. Mech. Phys. Solids 13 (4), 213–222.

Hornby, B., Schwartz, L., Hudson, J., 1994. Anisotropic effective-medium modeling of the elastic properties of shales. Geophysics 59 (October), 1570–1583.

Houtari, T., Kukkonen, I., 2004. Thermal expansion of rocks: literature survey and estimation of thermal expansion coefficient for olkiluoto mica gneiss. Working report. Geological Survey of Finland.

Katahara, K., 1996. Clay minerals elastic properties. In: Proceedings of the 66th SEG Annual Meeting, Expanded Technical Program Abstracts, pp. 1691–1694.

Khadeeva, Y., Vernik, L., 2014. Rock-physics model for unconventional shales. The Leading Edge 33 (3), 221–360.

Kroner, E., 1958. Berechnung derelastischen konstanten des vielkristalls aus den konstanten des einkristalls. Z. Phys. A Hadrons Nucl. 151 (4), 504–518.

Malthe-Srenssen, A., Jamtveit, B., Meakin, P., 2006. Fracture patterns generated by diffusion controlled volume changing reactions. Phys. Rev. Lett. (June), 96.

Mavko, G., Mukerji, T., Dvorkin, J., 2003. In: Rock Physics Handbook: Tools for Seismic Analysis in Porous mediaCambridge University Press, New York, USA.

McKinstry, H., 1965. Thermal expansion of clay minerals. Am. Mineral., 50.

Mori, T., Tanaka, K., 1973. Average stress in matrix and average elastic energy of materials with misfitting inclusions. Acta Metall. 21 (5), 571–574.

Ortega, J., Ulm, F.-J., Abousleiman, Y., 2009a. The effect of particle shape and grain-scale properties of shale: a micromechanics approach. Int. J. Numer. Anal. Methods Geomech. 34 (October), 1124–1156.

Ortega, J., Ulm, F.-J., Abousleiman, Y., 2009b. The nanogranular acoustic signature of shale. Geophysics 74, 3.

Pierson, O., 1993. Handbook of Carbon, Graphite, Diamond, and Fullerenes. Noyes Publications, New Jersey, USA.

Prasad, M., Mukerji, T., Reinstaedtler, M., GmbH, R., Arnold, W., 2009. Acoustic signatures, impedance microstructure, textural scales, and anisotropy of kerogen-rich shale, 533–543. SPE-124840-MS, DOI: http://dx.doi.org/10.2118/124840-MS.

Prioul, R., Donald, A., Koepsell, R., El Marzouki, Z., Bratton, T., 2007. Forward modeling of fracture-induced sonic anisotropy using a combination of borehole image and sonic logs. Geophysics 72 (4), E135–E147.

Qu, J., 1993a. The effect of slightly weakened interfaces on the overall elastic properties of composite materials. Mech. Mater. 14 (4), 269–281.

Qu, J., 1993b. Eshelby tensor for an elastic inclusion with slightly weakened interface. J. Appl. Mech. 60 (4), 1048–1050.

Radjai, F., Jean, M., Moreau, J.-J., Roux, S., 1996. Force distribution in dense two-dimensional granular systems. Phys. Rev. Lett. 77 (July (2)).

Romero, A., Philp, R., 2012. Organic geochemistry of the Woodford shale, Southwestern Oklahoma: How variable can shale be? AAPG Bull. 96 (3), 493–517.

Sayers, C., 2013. The effect of kerogen on the elastic anisotropy of organic-rich shales. Geophysics 78 (March–April (2)), D65–D74.

Seo, Y.-S., Ichikawa, Y., Kawamura, K., 1999. Stress–strain response of rock-forming minerals by md simulations. Mater. Sci. Res. Int. 5, 13–20.
Sorrell, C., Anderson, H., Ackermann, R., 1974. Thermal expansion and the high-low transformation in quartz. ii. Dilatometric studies. J. Appl. Cryst. 7 (468).
Thiercelin, M., Plumb, R., 1994. Core-based prediction of lithologic stress contrasts in East Texas formations. SPE Formation Evaluation, December.
Thomsen, L., 1986. Weak elastic anisotropy. Geophysics 51 (10), 195–196.
Ulm, F.-J., Abousleiman, Y., 2006. The nanogranular nature of shale. Acta Geotech. 1 (265), 77–88.
Ulm F.-J., Constantinides G., Delafargue A., Abousleiman Y., Ewy R., Duranti L. and McCarty D., Material invariant poromechanics properties of shales 37 (265), 2004, 43–58, Proceedings of the 3rd Biot Conference on Poromechanics, 24-27 May 2005, Norman, Oklahoma, USA. Edited by Franz-Josef Ulm, Younane N. Abousleiman, and Alexander H.-D. Cheng, http://dx.doi.org/10.1201/NOE0415380416.ch96.
Vaughan, M., Guggenheim, S., 1986. Elasticity of muscovite and its relationship to crystal structure. J. Geophys. Res. 91, 4657–4664.
Vernik, L., 1993. Microcrack-induced versus intrinsic elastic anisotropy in mature hc-source shales. Geophysics 58 (11), 1703–1706.
Vernik, L., Kachanov, M., 2010. Modeling elastic properties of siliciclastic rocks. Geophysics 75 (6), E171–E182.
Vernik, L., Landis, C., 1996. Elastic anisotropy of source rocks: implications for hydrocarbon generation and primary migration. AAPG Bull. 80 (4), 531–544.
Vernik, L., Nur, A., 1992. Ultrasonic velocity and anisotropy of hydrocarbon source rocks. Geophysics 57 (5), 727–735.
Vernik, L., Xingzhou, L., 1997. Velocity anisotropy in shales: a petrophysical study. Geophysics 62 (2), 521–532.
Yakobson, B., 1991. Morphology and rate of fracture in chemical decomposition of solids. Phys. Rev. Lett. 67 (September (12)).
Zaoui, A., 2002. Continuum micromechanics: a survey. J. Eng. Mech. 128 (August (8)), 808–816.
Zhang, L., Leboeuf, E., 2007. A molecular dynamics study of natural organic matter: 1. Lignin, kerogen and soot. Org. Chem. 40, 1132–1142.
Zhang, L., Leboeuf, E., Xing, B., 2007. Thermal analytical investigation of biopolymers and humic-and carbonaceous-based soil and sediment organic matter. Environ. Sci. Technol. 41 (14), 4888–4894.